Highly oxygenated organic molecule formation from 2,5-dimethylfuran oxidation by O_3 and OH: an experimental and computational study

Rabbia Asgher[1,★], Sakshi Jha[1,★], Avinash Kumar[1], Shawon Barua[1], Prasenjit Seal[1], Sana Farhoudian[1], Siddharth Iyer[1], and Matti Rissanen[1,2]

[1]Aerosol Physics Laboratory, Physics Unit, Tampere University, 33720 Tampere, Finland
[2]Department of Chemistry, University of Helsinki, 00560 Helsinki, Finland
★These authors contributed equally to this work.

Correspondence: Rabbia Asgher (rabbia.asgher@tuni.fi), Sakshi Jha (sakshi.jha@tuni.fi), and Matti Rissanen (matti.rissanen@tuni.fi)

S1. Experimental Setup

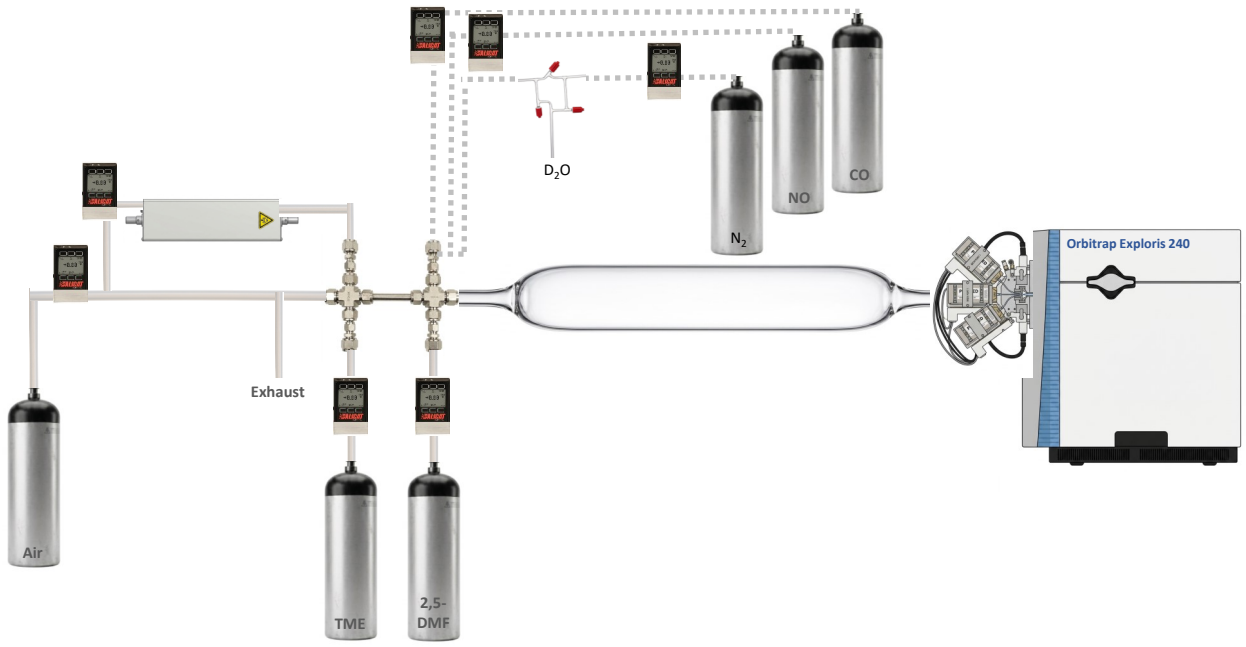

Figure S1. Schematic of the experimental setup used for the gas-phase oxidation of 2,5-dimethylfuran (2,5-DMF). Oxidation reactions were conducted in two separate horizontal flow tube reactors to investigate different reaction timescales. A borosilicate glass reactor (i.d. 2.2 cm) was used for short-residence-time experiments (0.8 s), while a larger borosilicate reactor (i.d. 4.7 cm) was employed for long-residence-time experiments (7 s). Precursor 2,5-DMF was introduced from a premixed gas cylinder (134 ppm in N_2) into the carrier air flow. O_3 was produced via UV photolysis of zero air ($\lambda = 185$ nm) and OH was generated in situ or via O_3 + tetramethylethylene (TME) reactions. Oxygenated products were analyzed using an Orbitrap Exploris 240 mass spectrometer equipped with a nitrate-based (NO_3^-) multi-scheme chemical ionization (MION) inlet. Selective chemistry was performed using NO to intercept RO_2 radicals, CO as an OH scavenger, and D_2O for hydrogen–deuterium (H/D) exchange. All gas flows were regulated using calibrated mass flow controllers (MFCs).

S2. Chemical purities and gas cylinder specifications

The following chemicals and compressed gases were utilized in the experiments: 2,5-dimethylfuran (2,5-DMF; C_6H_8O, ThermoFisher Scientific, 99% purity) was used to prepare a custom premixed gas cylinder containing 134 ppmv of the precursor diluted in high-purity nitrogen (N_2). Nitric oxide (NO), used for RO_2 radical interception experiments, was supplied as a certified 100 ppmv mixture in N_2 (Air Products). Carbon monoxide (CO), employed as a selective OH scavenger, was provided as a certified gas mixture at a concentration of 4500 ppmv (0.45%) in N_2 (Linde Oy). Tetramethylethylene (TME; 2,3-dimethyl-2-butene, 99% purity) was obtained from Sigma-Aldrich and used for in situ OH generation via ozonolysis.

Ozone (O_3) was generated by the 185 nm photolysis of purified zero air, provided by an AADCO 737-15 pure air generator, using a low-pressure mercury lamp (UVP, Analytik Jena). The ozone concentration was monitored using a 2B Technologies (model 205) ozone monitor. High-purity nitrogen (N_2, grade 5.0) and synthetic air were sourced from Woikoski Oy and Linde Oy. For hydrogen–deuterium (H/D) exchange experiments, deuterium oxide (D_2O, 99.9 atom % D, Sigma-Aldrich) was introduced into the flow reactor by bubbling high-purity N_2 through a liquid D_2O reservoir, allowing for the identification of labile hydrogen atoms (–OH and –OOH groups) in the oxidation products.

S3. CO perturbation experiments

CO perturbation experiments were performed at $\Delta t = 7$ s to isolate the ozonolysis and OH-initiated contributions to 2,5-DMF oxidation. CO was introduced as a selective OH scavenger ($CO + OH \rightarrow CO_2 + HO_2$) at 9.97×10^5 ppbv, with [2,5-DMF] stepped from 848 to 424 ppbv and [O_3] = 54 ppbv (Fig. S2). The OH-derived monomers $C_6H_9O_6$ and $C_6H_9O_8$ attenuate strongly while the ozonolysis-derived $C_6H_7O_7$ and $C_6H_7O_9$ persist (Fig. S2a), and the C_{10}–C_{11} accretion products are suppressed near-completely (Fig. S2b). This confirms that the OH-derived monomers and the C_{11} accretion product depend on the OH channel, whereas ozonolysis-driven RO_2 autoxidation sustains $C_6H_7O_x$ monomer formation independently of OH. The channel origin of the C_{10} accretion product compositions cannot be assigned from this data alone.

The same separation appears in the spectrum with OH supplied via in situ VHP decomposition and external TME ozonolysis (Fig. S3, $\Delta t = 7$ s). The $C_6H_7O_6$–$C_6H_7O_9$ series persists under CO, confirming ozonolysis-driven RO_2 autoxidation continues independently of OH. $C_6H_9O_6$ and $C_6H_9O_8$ are markedly attenuated relative to the CO-free spectrum (Fig. 3b), and no C_{10}–C_{12} accretion products appear.

S4. Other Possible Pathways Explored for O_3- and OH-Initiated Oxidation of 2,5-Dimethylfuran

This section summarizes additional reaction pathways explored at different stages of the reaction network. All calculations were performed at the M06-2X/6-31G(d,p) level of theory. Pathways exhibiting comparatively low energy barriers and atmospheric relevance are discussed in the main manuscript, whereas the pathways presented here were found to be kinetically uncompetitive and are therefore not expected to contribute significantly under atmospheric conditions.

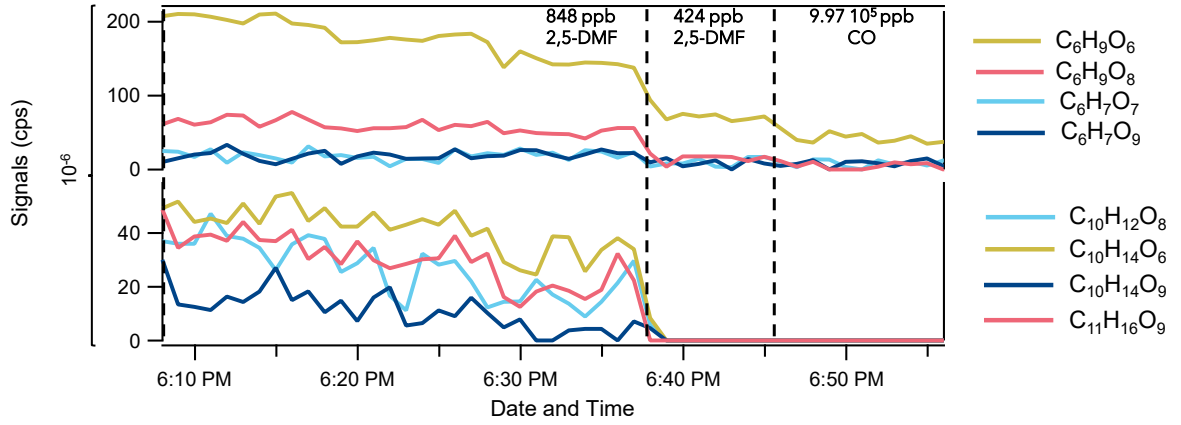

Figure S2. Time series of O_3- and OH-derived oxidation products during CO perturbation experiments. CO was introduced at 9.97×10^5 ppbv as a selective OH scavenger ($CO + OH \rightarrow CO_2 + HO_2$), suppressing OH-initiated ring addition while leaving ozonolysis intact. CO addition also elevates HO_2, shifting bimolecular RO_2 termination toward hydroperoxide (ROOH) formation. (a) The OH-derived monomers $C_6H_9O_6$ and $C_6H_9O_8$ attenuate strongly under CO while the ozonolysis-derived $C_6H_7O_7$ and $C_6H_7O_9$ persist. (b) The accretion products $C_{10}H_{12}O_8$, $C_{10}H_{14}O_6$, $C_{10}H_{14}O_9$, and $C_{11}H_{16}O_9$ are suppressed near-completely under CO. Experimental conditions: [2,5-DMF] = 848 ppbv and 424 ppbv, [O_3] = 54 ppbv, $\Delta t = 7$ s.

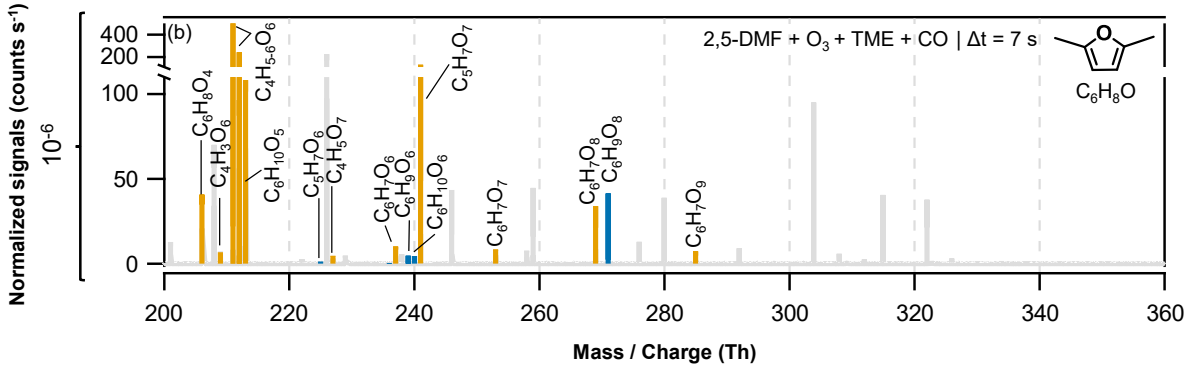

Figure S3. NO_3^- CIMS mass spectrum of 2,5-DMF oxidation by O_3 and OH under CO at $\Delta t = 7$ s, with OH supplied via in situ VHP decomposition and external TME ozonolysis. [2,5-DMF] = 169 ppbv, [O_3] = 54 ppbv, [TME] = 21 ppbv, [CO] = 9.97×10^5 ppbv. Peak labels indicate assigned neutral molecular compositions (NO_3^- adduct excluded). O_3-derived monomers ($C_6H_7O_x$) shown in yellow, OH-derived monomers ($C_6H_9O_x$) in blue. The $C_6H_7O_6$–$C_6H_7O_9$ series persists under CO, confirming ozonolysis-driven RO_2 autoxidation continues independently of OH. $C_6H_9O_6$ and $C_6H_9O_8$ are markedly attenuated relative to the CO-free spectrum (Fig. 3b), and no C_{10}–C_{12} accretion products appear.

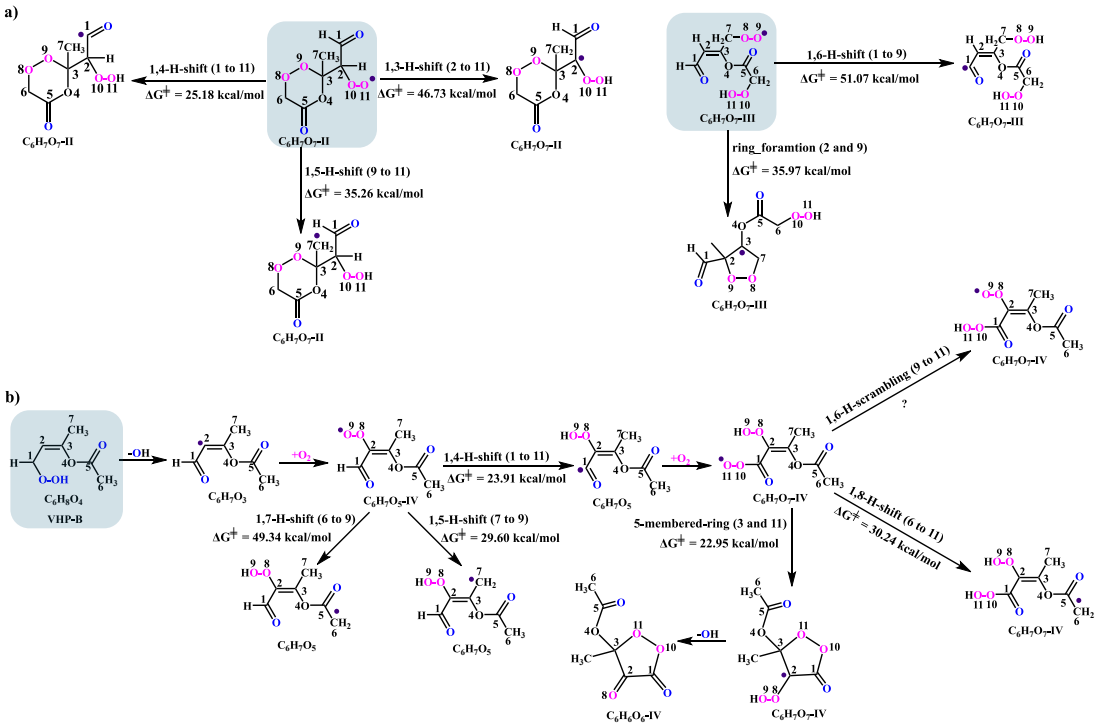

Figure S4. (a) Additional explored reaction channels for the $C_6H_7O_7$ structures II and III, as defined in the main manuscript. (b) Additional explored reaction channels originating from VHP-B, including 1,x-H shifts ($x = 3$–8) and ring-closure pathways. Barrier heights ($\Delta G^{\ddagger}$, kcal mol^{-1}) were calculated at the M06-2X/6-31G(d,p) level of theory. A question mark (?) indicates that the corresponding transition state could not be located. Colour code: pink oxygen atoms represent O_2 addition.

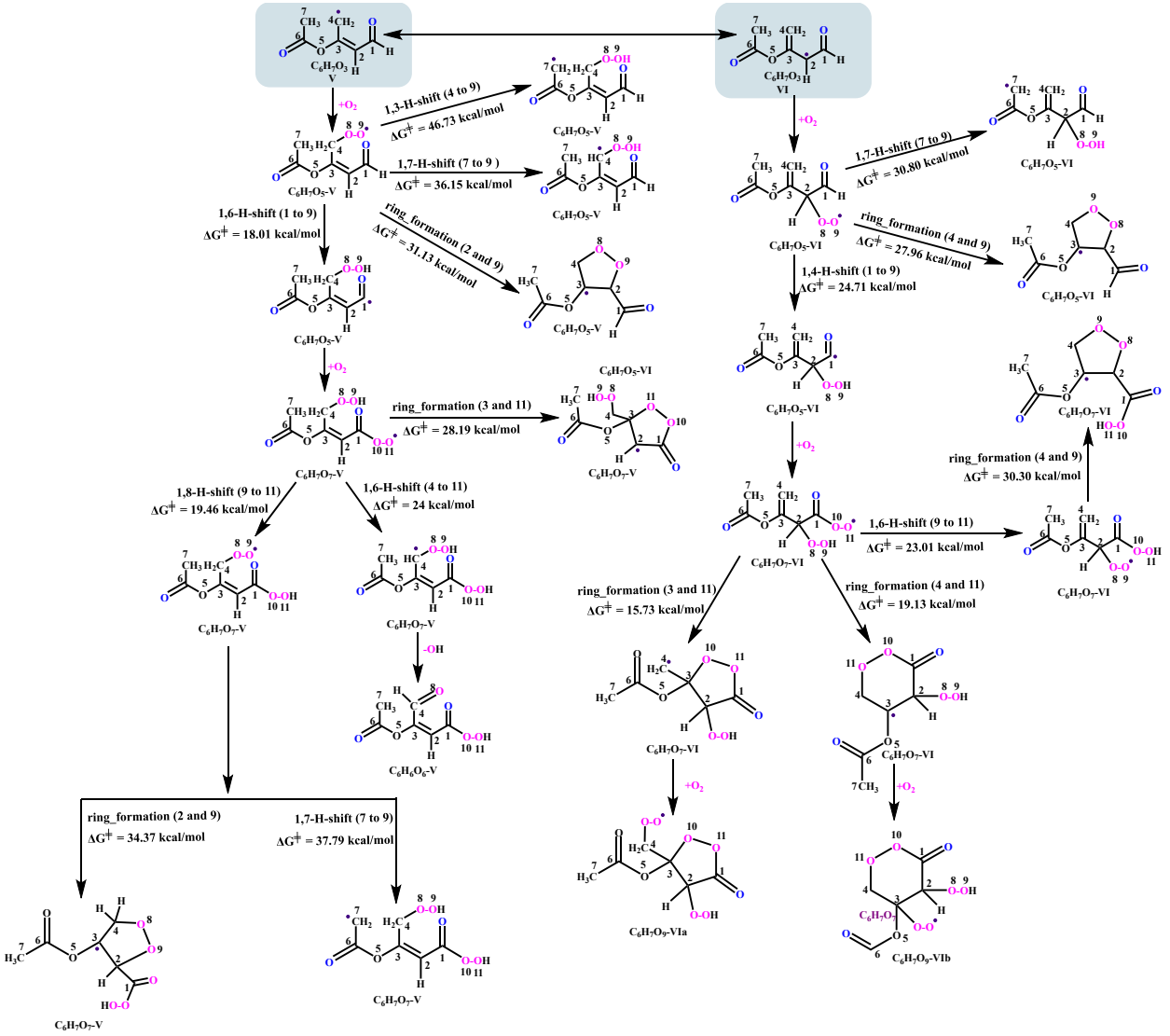

Figure S5. All explored reaction channels originating from the VHP-C-derived structures V and VI ($C_6H_7O_3$), including 1,x-H shifts ($x = 3$–8) and ring-closure pathways. Barrier heights ($\Delta G^{\ddagger}$, kcal mol^{-1}) for all structures were calculated at the M06-2X/6-31G(d,p) level of theory. Colour code: pink oxygen atoms represent O_2 addition.

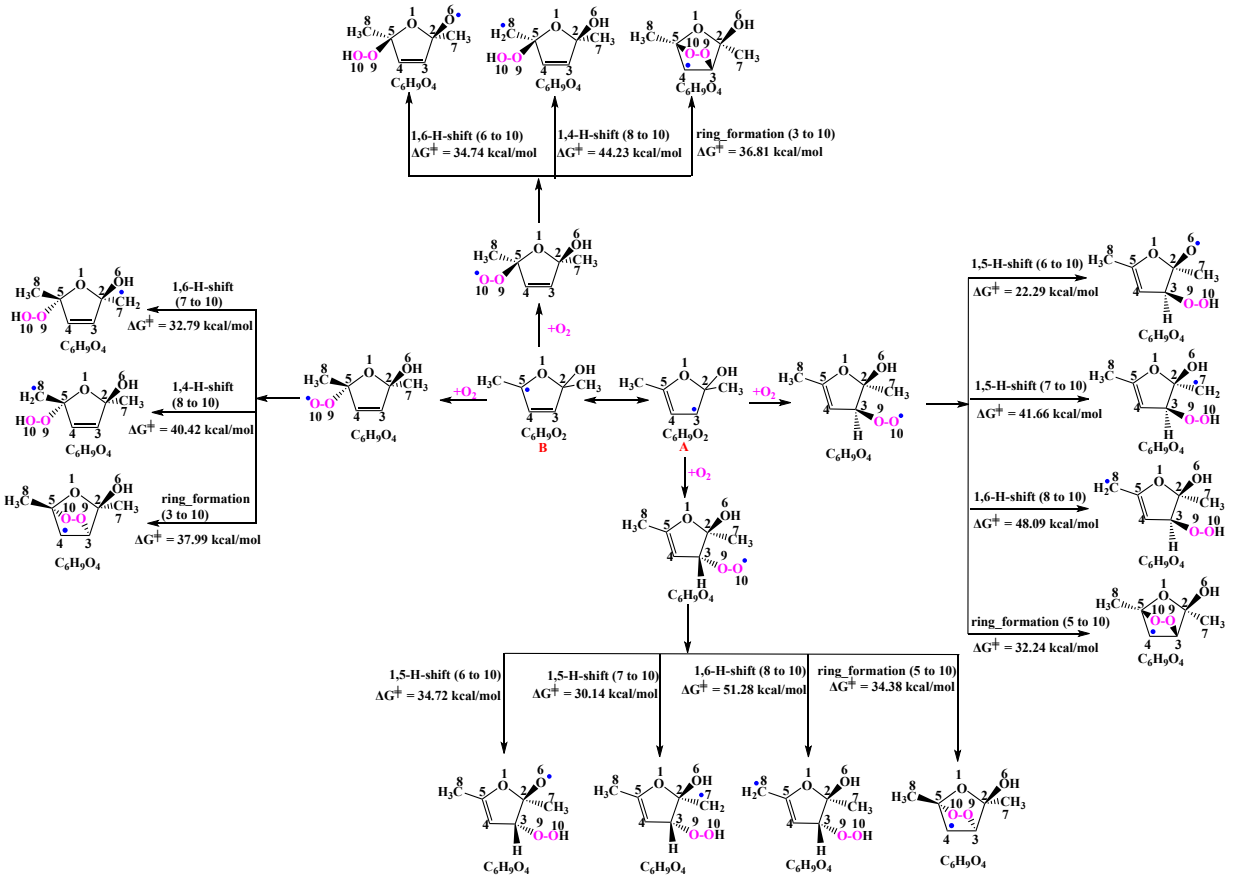

Figure S6. All explored reaction channels originating from the $C_6H_9O_2$ radical formed following OH addition at the 2-position of 2,5-DMF. The figure shows pathways starting from structure A and its resonance form B, illustrating the mechanistic channels considered from this intermediate, including 1,x-H shifts ($x = 4$–6) and ring-closure pathways. Barrier heights ($\Delta G^{\ddagger}$, kcal mol^{-1}) for all structures were calculated at the M06-2X/6-31G(d,p) level of theory. Colour code: pink oxygen atoms represent O_2 addition.

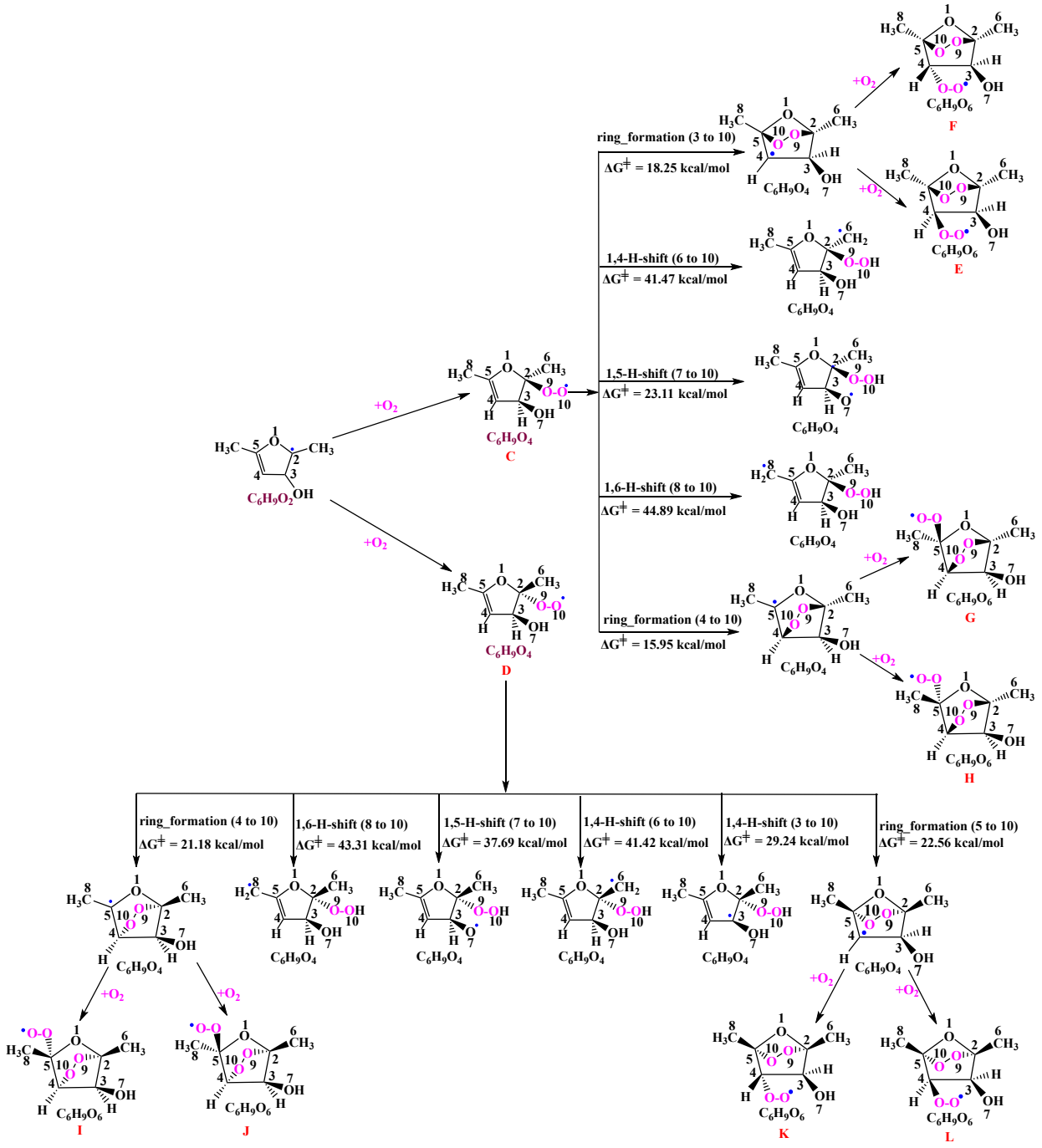

Figure S7. All explored reaction channels for the $C_6H_9O_2$ radical formed following OH addition at the 3-position of the 2,5-DMF ring. The figure illustrates pathways originating from the initial radical intermediates C and D, including intramolecular 1,x-H shifts ($x = 4$–6) and endo/exo cyclization (ring-formation) reactions. Most of the investigated pathways involve energy barriers that are too high to be relevant under atmospheric conditions and are therefore not expected to be kinetically competitive. Among the explored channels, only those leading to intermediates E, F, G, H, I, J, K, and L are kinetically accessible and can result in the formation of $C_6H_9O_6$ (O_6-HOM species). Barrier heights ($\Delta G^{\ddagger}$, kcal mol^{-1}) were calculated at the M06-2X/6-31G(d,p) level of theory. Colour code: pink oxygen atoms represent O_2 addition.

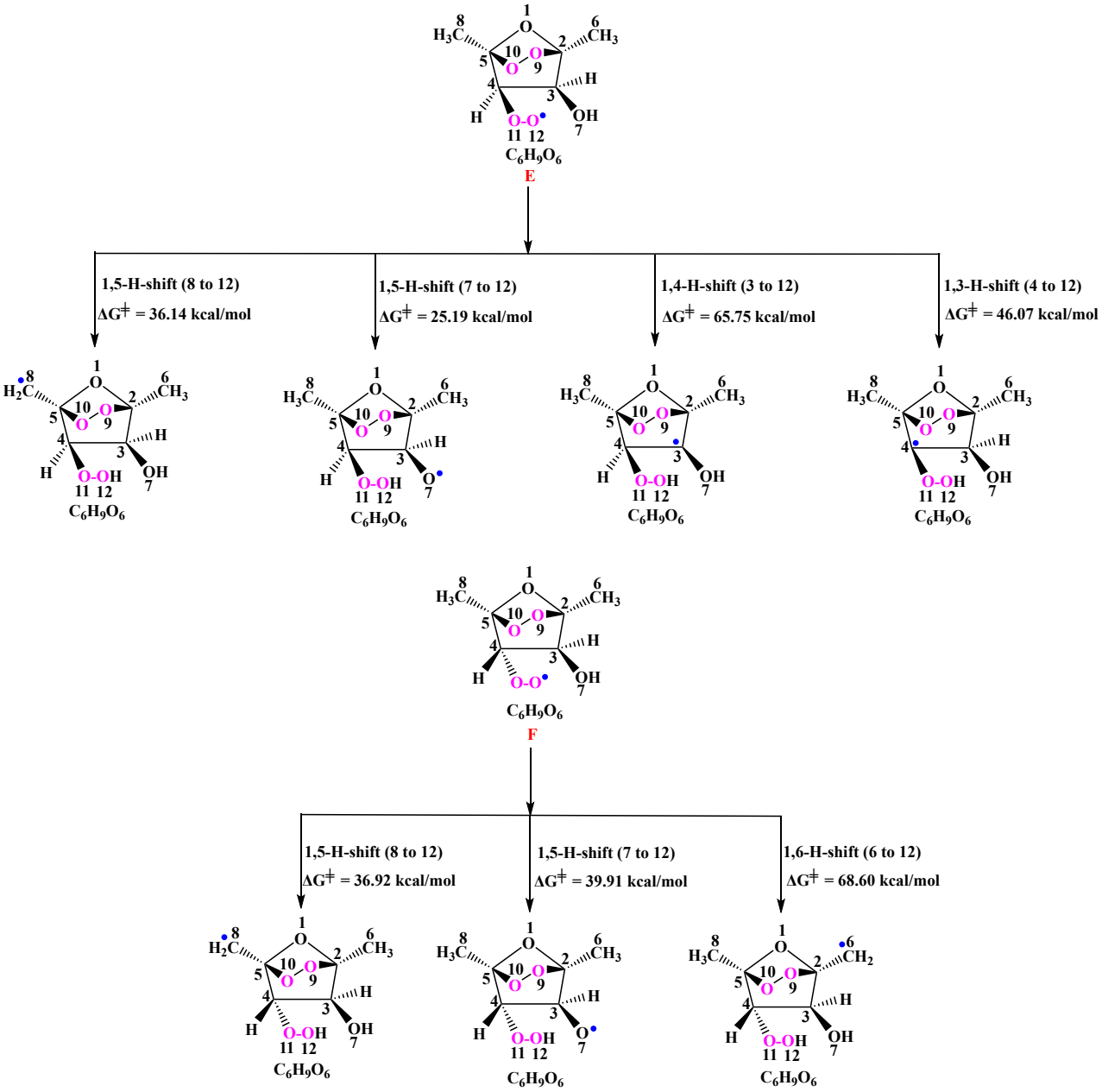

Figure S8. Continuation of the reaction network shown in Figure S7, illustrating additional reaction channels originating from the $C_6H_9O_6$ intermediates E and F via intramolecular 1,x-H shifts ($x = 3$–6). Barrier heights ($\Delta G^{\ddagger}$, kcal mol^{-1}) were calculated at the M06-2X/6-31G(d,p) level of theory. All explored pathways exhibit relatively high barriers and are therefore not expected to be kinetically competitive under atmospheric conditions for the formation of HOM species up to O_8. Colour code: pink oxygen atoms represent O_2 addition.

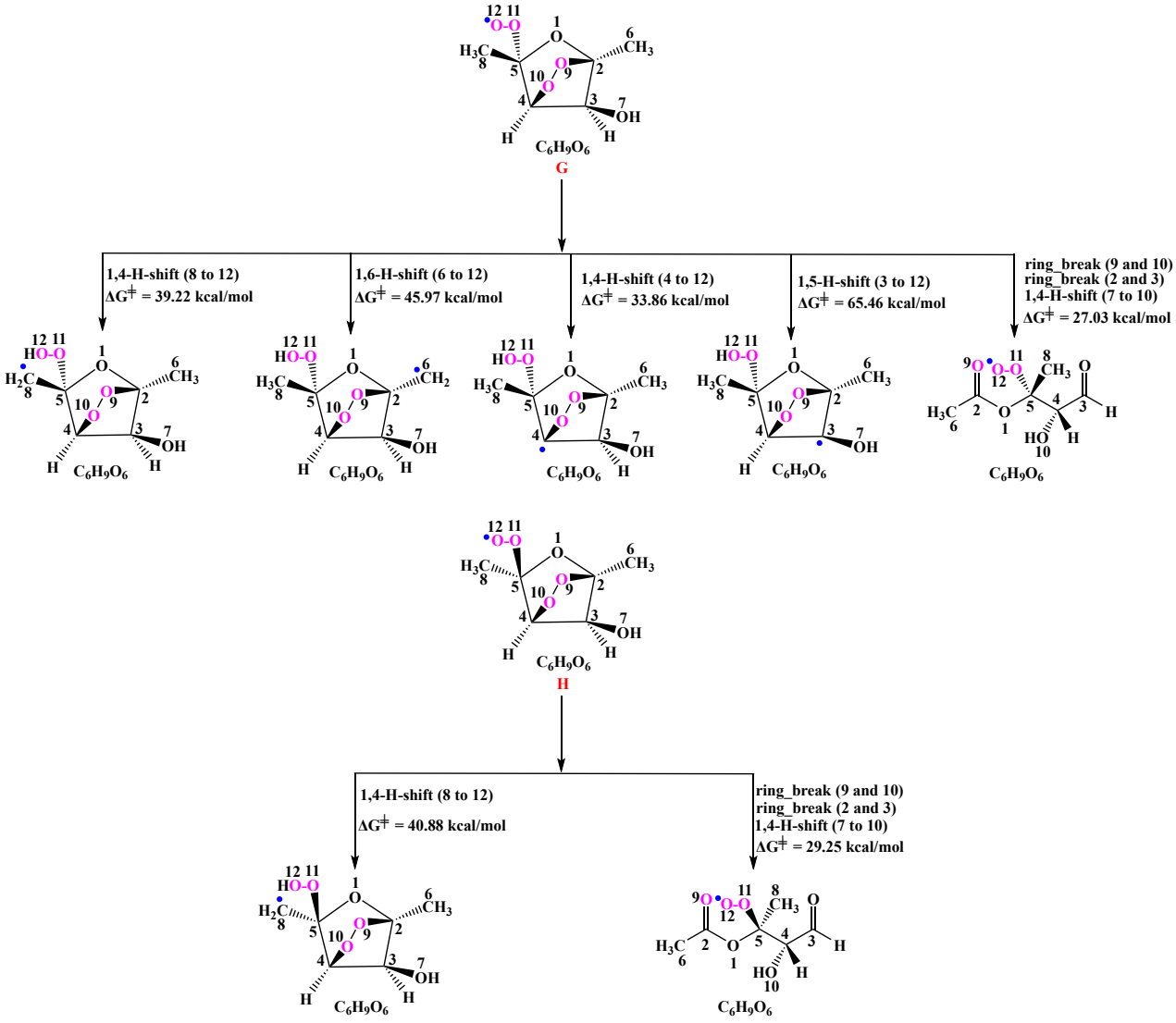

Figure S9. Continuation of the reaction network shown in Figure S7, illustrating additional reaction channels originating from the $C_6H_9O_6$ intermediates G and H via intramolecular 1,x-H shifts ($x = 4$–6), including ring-breaking pathways.Barrier heights ($\Delta G^{\ddagger}$, kcal mol^{-1}) were calculated at the M06-2X/6-31G(d,p) level of theory. All explored pathways exhibit relatively high barriers and are therefore not expected to be kinetically competitive under atmospheric conditions for the formation of HOM species up to O_8. Colour code: pink oxygen atoms represent O_2 addition.

S5. Kinetic modelling of CI-derived O_9 formation

As discussed in the main manuscript, kinetic modelling was performed using Kinetiscope to evaluate the influence of the Anti-CI-2A geometry on HOM formation, particularly the formation of O_9 species. First, POZ decomposition was simulated for 7 s using the experimental concentrations (1360 ppbv 2,5-DMF and 117 ppbv O_3, corresponding to the short residence-time experiment of 0.8 s), as illustrated in Reaction Scheme 1. The average concentration of POZ formed is summarized in Table S1. To ensure adequate sampling of reaction events, simulations were performed using total particle number settings of 1×10^7 and 1×10^8, thereby assessing the sensitivity of the results to the chosen total particle number. A random number seed of 28224 was used for all simulations, ensuring that the same sequence of random events was employed in each simulation.

Reaction Scheme 1:

$$2,5\text{-DMF} + O_3 \rightarrow \text{POZ} \qquad (k = 5.03 \times 10^{-16}\ \text{cm}^3\ \text{molecule}^{-1}\ \text{s}^{-1})$$

Table S1. Model input concentrations of 2,5-DMF and O_3, and the corresponding simulated POZ concentrations obtained under different total particle number settings (1×10^7 and 1×10^8) using a random number seed of 28224.

Species	**Model Input** (molecule cm^{-3})	**Model Output** Average concentration (molecule cm^{-3})
Simulation settings with a total particle number of 10^7		
2,5-DMF	3.35 $\times 10^{13}$	-
O_3	2.88 $\times 10^{12}$	-
POZ	-	1.60 $\times 10^{11}$
Simulation settings with a total particle number of 10^8		
2,5-DMF	3.35 $\times 10^{13}$	-
O_3	2.88 $\times 10^{12}$	-
POZ	-	1.59 $\times 10^{11}$

In the second reaction scheme, two additional reaction steps describing the decomposition of POZ to Syn-CI-1 and Syn-CI-2 were included. Both the TST rate coefficients calculated in this study (k^{i}) and the rate coefficients adjusted to reproduce the MESMER branching ratio, thereby accounting for the excess energy retained in the chemically activated POZ (k^{ii}), are listed in Reaction Scheme 2 and Table S2.

Reaction Scheme 2:

$$\begin{aligned}
&2,5\text{-DMF} + O_3 \rightarrow \text{POZ} && (k = 5.03 \times 10^{-16}\ \text{cm}^3\ \text{molecule}^{-1}\ \text{s}^{-1})\\
&\text{POZ} \rightarrow \text{Syn-CI-1} && (k = {}^{\text{i}}4.28 \times 10^{1};\ {}^{\text{ii}}1.04 \times 10^{4}\ \text{s}^{-1})\\
&\text{POZ} \rightarrow \text{Syn-CI-2} && (k = {}^{\text{i}}1.89 \times 10^{5};\ {}^{\text{ii}}1.79 \times 10^{5}\ \text{s}^{-1})
\end{aligned}$$

[i] TST rate coefficients calculated in this study. [ii] Rate coefficients adjusted to reproduce the MESMER branching ratio (≈5.5% Syn-CI-1 and ≈94.5% Syn-CI-2)

Table S2. Model input concentrations of 2,5-DMF and O_3 and the corresponding simulated concentrations of POZ, Syn-CI-1, and Syn-CI-2 obtained at two total particle number settings (1×10^7 and 1×10^8) using a random number seed of 28224.

Species	**Model Input** (molecule cm^{-3})	**Model Output** Average concentration (molecule cm^{-3})
Simulation settings with a total particle number of 10^7		
2,5-DMF	3.35×10^{13}	–
O_3	2.88×10^{12}	–
POZ	–	[i] 3.99×10^5; [ii] 3.99×10^5
Syn-CI-1	–	[i] 4.5×10^7; [ii] 9.03×10^9
Syn-CI-2	–	[i] 1.6×10^{11}; [ii] 1.50×10^{11}
Simulation settings with a total particle number of 10^8		
2,5-DMF	3.35×10^{13}	–
O_3	2.88×10^{12}	–
POZ	–	[i] 3.69×10^5; [ii] 3.69×10^5
Syn-CI-1	–	[i] 3.47×10^7; [ii] 8.83×10^9
Syn-CI-2	–	[i] 1.59×10^{11}; [ii] 1.51×10^{11}

[i] Average concentrations obtained using the TST rate coefficients calculated in this study. [ii] Average concentrations obtained using the MESMER-adjusted rate coefficients, accounting for the excess energy retained in the chemically activated POZ (≈5.5% Syn-CI-1 and ≈94.5% Syn-CI-2).

For the simulations with total particle numbers of 1×10^7 and 1×10^8, the 7 s time-averaged species distributions were nearly identical using both the TST and MESMER-adjusted rate coefficients. The average populations of Syn-CI-1, Syn-CI-2, and POZ differed by less than 0.4 percentage points between the two particle number settings, indicating that the simulated species distributions are not significantly affected by the chosen total particle number. Based on these results, all subsequent simulations were performed using the 1×10^8 total particle number setting to improve sampling of low-probability reaction events and reduce stochastic variability.

The CI populations obtained from Reaction Scheme 2 were then used as initial conditions in another simplified reaction scheme (Reaction Scheme 3) initiated directly from the Criegee intermediates (CI) concentrations (Table S2). The rate coefficients used in the scheme were obtained from calculations performed in this study using the MC-TST method. The OH-loss step was described using a literature-based rate coefficient of approximately 10^7 s^{-1}, representing the fast unimolecular decay of hydroperoxide intermediates formed following Criegee intermediate formation (Fang et al., 2016). O_2 addition was treated as a pseudo-unimolecular process using a rate coefficient of approximately 10^7 s^{-1}, reflecting the rapid association of molecular oxygen with carbon-centered radical intermediates under atmospheric conditions. In addition, bimolecular rate coefficients for radical–radical recombination reactions, including RO_2 + RO_2 and cross-reactions among the formed radical species, were

assigned a generic literature value of 3.20×10^{-11} cm^3 molecule^{-1} s^{-1} to represent their role as sink processes in the kinetic model (Barua et al., 2026; Berndt et al., 2018).

Equal populations of the corresponding Syn and Anti conformers were assumed for both CI-1 and CI-2, based on the average Syn-CI concentrations predicted by Reaction Scheme 2 using the TST and MESMER-adjusted rate coefficients. To evaluate the potential role of Anti-CI-2A in HOM formation, kinetic simulations were performed by introducing this conformer at 0.01% of the average POZ concentration obtained from Reaction Scheme 1, corresponding to 1.60×10^7 molecules cm^{-3} in both the conditions. Inclusion of this pathway resulted in the formation of VHP-C and subsequently O_9 species well within the experimental timescale of 0.8 s. To assess stochastic variability, simulations were repeated using different random number seeds (28224, 11752, 26138, 11284, and 21542), and the results are summarized in Table S3. Of the two possible O_9 products shown in Figure 9 of the main manuscript, only $C_6H_7O_9$-VIa was observed in the simulations. Its onset time varied between 0.002 and 0.064 s among simulations, while the predicted concentrations remained approximately within the same order of magnitude 10^5 molecules cm^{-3}. These results suggest that even a minor contribution from Anti-CI-2A may be sufficient to account for O_9 formation within the experimental timescale under the simulated conditions.

Table S3. Onset times and average concentrations of $C_6H_7O_9$-VIa obtained from kinetic simulations using different random number seeds at a total particle number setting of 1×10^8.

28224		
Species	**Onset time (s)**	**Average particle number concentration (molecule cm^{-3})**
$C_6H_7O_9$-VIa	0.002^{i}; 0.045^{ii}	$^{i}1.10 \times 10^{05}$; $^{ii}1.01 \times 10^{05}$
11752		
Species	**Onset time (s)**	**Average particle number concentration (molecule cm^{-3})**
$C_6H_7O_9$-VIa	0.015^{i}; 0.055^{ii}	$^{i}1.33 \times 10^{05}$; $^{ii}1.32 \times 10^{05}$
26138		
Species	**Onset time (s)**	**Average particle number concentration (molecule cm^{-3})**
$C_6H_7O_9$-VIa	0.008^{i}; 0.036^{ii}	$^{i}1.08 \times 10^{05}$; $^{ii}1.17 \times 10^{05}$
11284		
Species	**Onset time (s)**	**Average particle number concentration (molecule cm^{-3})**
$C_6H_7O_9$-VIa	0.064^{i}; 0.045^{ii}	$^{i}1.55 \times 10^{05}$; $^{ii}1.56 \times 10^{05}$
21542		
Species	**Onset time (s)**	**Average particle number concentration (molecule cm^{-3})**
$C_6H_7O_9$-VIa	0.057^{i}; 0.045^{ii}	$^{i}9.91 \times 10^{04}$; $^{ii}1.01 \times 10^{05}$

[i] Onset times and average concentrations calculated using the initial CI populations obtained from Reaction Scheme 2 with the TST rate coefficients. [ii] Onset times and average concentrations calculated using the initial CI populations obtained from Reaction Scheme 2 with the MESMER-adjusted rate coefficients, thereby accounting for the excess energy retained in the chemically activated POZ (≈5.5% Syn-CI-1 and ≈94.5% Syn-CI-2).

Reaction scheme 3:

1. *Syn*$-$CI$-1 \rightarrow$ VHP$-$A ($k = 5.92 \times 10^{+02}$)
   (Input concentration of Syn-CI-1: [i]3.47×10^{7}; [ii]8.83×10^{9} molecules cm^{-3})
2. *Syn*$-$CI$-1 \rightarrow$ DI_ox_CI1 ($k = 8.81 \times 10^{+04}$)
3. *Anti*$-$CI$-1 \rightarrow$ MEM_6 ($k = 2.02 \times 10^{-04}$)
   (Input concentration of Anti-CI-1: [i]3.47×10^{7}; [ii]8.83×10^{9} molecules cm^{-3})
4. *Anti*$-$CI$-1 \rightarrow$ SOZ ($k = 1.02 \times 10^{+08}$)
5. VHP$-$A $\rightarrow$ OH + VHP$-$A_O3 ($k = 1.00 \times 10^{+07}$)
6. VHP$-$A_O3 $\rightarrow$ VHP$-$A_O5 ($k = 1.00 \times 10^{+07}$)
7. 2 VHP$-$A_O5 $\rightarrow$ sink_1 ($k = 3.20 \times 10^{-11}$)
8. VHP$-$A_O5 $\rightarrow$ VHP$-$A_O5_1_7_H_rad ($k = 1.63 \times 10^{-03}$)
9. VHP$-$A_O5_1_7_H_rad $\rightarrow$ VHP$-$A_O7 ($k = 1.00 \times 10^{+07}$)
10. 2 VHP$-$A_O7 $\rightarrow$ sink_2 ($k = 3.20 \times 10^{-11}$)
11. VHP$-$A_O7 + VHP$-$A_O5 $\rightarrow$ sink_3 ($k = 3.20 \times 10^{-11}$)
12. VHP$-$A_O5 $\rightarrow$ VHP$-$A_O5_rg_6_rad ($k = 3.04 \times 10^{-02}$)
13. VHP$-$A_O5_rg_6_rad $\rightarrow$ VHP$-$A_rg_6_O7 ($k = 1.00 \times 10^{+07}$)
14. 2 VHP$-$A_rg_6_O7 $\rightarrow$ sink_4 ($k = 3.20 \times 10^{-11}$)
15. VHP$-$A_rg_6_O7 + VHP$-$A_O7 $\rightarrow$ sink_5 ($k = 3.20 \times 10^{-11}$)
16. VHP$-$A_rg_6_O7 + VHP$-$A_O5 $\rightarrow$ sink_6 ($k = 3.20 \times 10^{-11}$)
17. VHP$-$A_O5 $\rightarrow$ VHP$-$A_O5_rg_7_rad ($k = 3.87 \times 10^{-04}$)
18. VHP$-$A_O5_rg_7_rad $\rightarrow$ VHP$-$A_rg_7_O7 ($k = 1.00 \times 10^{+07}$)
19. 2 VHP$-$A_rg_7_O7 $\rightarrow$ sink_7 ($k = 3.20 \times 10^{-11}$)
20. VHP$-$A_rg_7_O7 + VHP$-$A_rg_6_O7 $\rightarrow$ sink_8 ($k = 3.20 \times 10^{-11}$)
21. VHP$-$A_rg_7_O7 + VHP$-$A_O7 $\rightarrow$ sink_9 ($k = 3.20 \times 10^{-11}$)
22. VHP$-$A_rg_7_O7 + VHP$-$A_O5 $\rightarrow$ sink_10 ($k = 3.20 \times 10^{-11}$)

23. *Syn*−CI−2 → DI_OX_CI2 ($k = 1.92 \times 10^{+00}$)
    (Input concentration of Syn-CI-2: [i] 1.59×10^{11}; [ii] 1.51×10^{11} molecules cm^{-3})

24. *Anti*−CI−2 → VHP−B ($k = 5.21 \times 10^{-01}$)
    (Input concentration of Anti-CI-2: [i] 1.59×10^{11}; [ii] 1.51×10^{11} molecules cm^{-3})

25. VHP−B → VHP−B_O5 ($k = 1.00 \times 10^{+07}$)

26. 2 VHP−B_O5 → sink_11 ($k = 3.20 \times 10^{-11}$)

27. VHP−B_O5 + VHP−A_rg_7_O7 → sink_12 ($k = 3.20 \times 10^{-11}$)

28. VHP−B_O5 + VHP−A_rg_6_O7 → sink_13 ($k = 3.20 \times 10^{-11}$)

29. VHP−B_O5 + VHP−A_O7 → sink_14 ($k = 3.20 \times 10^{-11}$)

30. VHP−B_O5 + VHP−A_O5 → sink_15 ($k = 3.20 \times 10^{-11}$)

31. VHP−B_O5 → VHP−B_O7_rad ($k = 9.33 \times 10^{-02}$)

32. VHP−B_O7_rad → VHP−B_O7 ($k = 1.00 \times 10^{+07}$)

33. VHP−B_O7 → VHP−B_rg_5_mol ($k = 4.47 \times 10^{-02}$)

34. VHP−B_rg_5_mol → VHP−B_C6H6O6 ($k = 1.00 \times 10^{+07}$)

35. 2 VHP−B_O7 → sink_16 ($k = 3.20 \times 10^{-11}$)

36. VHP−B_O7 + VHP−B_O5 → sink_17 ($k = 3.20 \times 10^{-11}$)

37. VHP−B_O7 + VHP−A_rg_7_O7 → sink_18 ($k = 3.20 \times 10^{-11}$)

38. VHP−B_O7 + VHP−A_rg_6_O7 → sink_19 ($k = 3.20 \times 10^{-11}$)

39. VHP−B_O7 + VHP−A_O7 → sink_20 ($k = 3.20 \times 10^{-11}$)

40. VHP−B_O7 + VHP−A_O5 → sink_21 ($k = 3.20 \times 10^{-11}$)

41. *Anti*−CI−2A → VHP−C ($k = 2.15 \times 10^{+07}$)
    (Input concentration of Anti-CI-2A: 1.60×10^{7} molecules cm^{-3})

42. *Anti*−CI−2A → *Anti*−CI−2A_rg_5_mol ($k = 1.69 \times 10^{+05}$)

43. VHP−C → OH + VHP−C_rad ($k = 1.00 \times 10^{+07}$)

44. VHP−C_rad → VHP−C_O5_1 ($k = 1.00 \times 10^{+07}$)

45. $2\,\mathrm{VHP{-}C\_O5\_1} \rightarrow \mathrm{sink\_22}$ ($k = 3.20 \times 10^{-11}$)

46. $\mathrm{VHP{-}C\_O5\_1} + \mathrm{VHP{-}A\_rg\_7\_O7} \rightarrow \mathrm{sink\_23}$ ($k = 3.20 \times 10^{-11}$)

47. $\mathrm{VHP{-}C\_O5\_1} + \mathrm{VHP{-}A\_rg\_6\_O7} \rightarrow \mathrm{sink\_24}$ ($k = 3.20 \times 10^{-11}$)

48. $\mathrm{VHP{-}C\_O5\_1} + \mathrm{VHP{-}A\_O7} \rightarrow \mathrm{sink\_25}$ ($k = 3.20 \times 10^{-11}$)

49. $\mathrm{VHP{-}C\_O5\_1} + \mathrm{VHP{-}A\_O5} \rightarrow \mathrm{sink\_26}$ ($k = 3.20 \times 10^{-11}$)

50. $\mathrm{VHP{-}C\_O5\_1} + \mathrm{VHP{-}B\_O5} \rightarrow \mathrm{sink\_27}$ ($k = 3.20 \times 10^{-11}$)

51. $\mathrm{VHP{-}C\_O5\_1} + \mathrm{VHP{-}B\_O7} \rightarrow \mathrm{sink\_28}$ ($k = 3.20 \times 10^{-11}$)

52. $\mathrm{VHP{-}C\_O5\_1} \rightarrow \mathrm{VHP{-}C\_O5\_1\_rad}$ ($k = 1.01 \times 10^{+03}$)

53. $\mathrm{VHP{-}C\_O5\_1\_rad} \rightarrow \mathrm{VHP{-}C\_O7\_1}$ ($k = 1.00 \times 10^{+07}$)

54. $2\,\mathrm{VHP{-}C\_O7\_1} \rightarrow \mathrm{sink\_29}$ ($k = 3.20 \times 10^{-11}$)

55. $\mathrm{VHP{-}C\_O7\_1} + \mathrm{VHP{-}C\_O5\_1} \rightarrow \mathrm{sink\_30}$ ($k = 3.20 \times 10^{-11}$)

56. $\mathrm{VHP{-}C\_O7\_1} + \mathrm{VHP{-}A\_rg\_7\_O7} \rightarrow \mathrm{sink\_31}$ ($k = 3.20 \times 10^{-11}$)

57. $\mathrm{VHP{-}C\_O7\_1} + \mathrm{VHP{-}A\_rg\_6\_O7} \rightarrow \mathrm{sink\_32}$ ($k = 3.20 \times 10^{-11}$)

58. $\mathrm{VHP{-}C\_O7\_1} + \mathrm{VHP{-}A\_O7} \rightarrow \mathrm{sink\_33}$ ($k = 3.20 \times 10^{-11}$)

59. $\mathrm{VHP{-}C\_O7\_1} + \mathrm{VHP{-}A\_O5} \rightarrow \mathrm{sink\_34}$ ($k = 3.20 \times 10^{-11}$)

60. $\mathrm{VHP{-}C\_O7\_1} + \mathrm{VHP{-}B\_O5} \rightarrow \mathrm{sink\_35}$ ($k = 3.20 \times 10^{-11}$)

61. $\mathrm{VHP{-}C\_O7\_1} + \mathrm{VHP{-}B\_O7} \rightarrow \mathrm{sink\_36}$ ($k = 3.20 \times 10^{-11}$)

62. $\mathrm{VHP{-}C\_O7\_1} \rightarrow \mathrm{VHP{-}C\_O7\_slow}$ ($k = 4.76 \times 10^{-04}$)

63. $\mathrm{VHP{-}C\_O7\_slow} \rightarrow \mathrm{VHP{-}C\_C6H6O6}$ ($k = 1.00 \times 10^{+07}$)

64. $\mathrm{VHP{-}C\_O7\_1} \rightarrow \mathrm{VHP{-}C\_O7\_h\_scram}$ ($k = 2.10 \times 10^{-01}$)

65. $2\,\mathrm{VHP{-}C\_O7\_h\_scram} \rightarrow \mathrm{sink\_37}$ ($k = 3.20 \times 10^{-11}$)

66. $\mathrm{VHP{-}C\_O7\_h\_scram} + \mathrm{VHP{-}C\_O7\_1} \rightarrow \mathrm{sink\_38}$ ($k = 3.20 \times 10^{-11}$)

67. $\mathrm{VHP{-}C\_O7\_h\_scram} + \mathrm{VHP{-}C\_O5\_1} \rightarrow \mathrm{sink\_39}$ ($k = 3.20 \times 10^{-11}$)

68. $\mathrm{VHP{-}C\_O7\_h\_scram} + \mathrm{VHP{-}A\_rg\_6\_O7} \rightarrow \mathrm{sink\_40}$ ($k = 3.20 \times 10^{-11}$)

69. VHP−C_O7_h_scram + VHP−A_rg_7_O7 → sink_41 ($k = 3.20 \times 10^{-11}$)

70. VHP−C_O7_h_scram + VHP−A_O7 → sink_42 ($k = 3.20 \times 10^{-11}$)

71. VHP−C_O7_h_scram + VHP−A_O5 → sink_43 ($k = 3.20 \times 10^{-11}$)

72. VHP−C_O7_h_scram + VHP−B_O5 → sink_44 ($k = 3.20 \times 10^{-11}$)

73. VHP−C_O7_h_scram + VHP−B_O7 → sink_45 ($k = 3.20 \times 10^{-11}$)

74. VHP−C_rad → VHP−C_O5_2 ($k = 1.00 \times 10^{+07}$)

75. 2 VHP−C_O5_2 → sink_46 ($k = 3.20 \times 10^{-11}$)

76. VHP−C_O5_2 + VHP−C_O7_h_scram → sink_47 ($k = 3.20 \times 10^{-11}$)

77. VHP−C_O5_2 + VHP−C_O7_1 → sink_48 ($k = 3.20 \times 10^{-11}$)

78. VHP−C_O5_2 + VHP−C_O5_1 → sink_49 ($k = 3.20 \times 10^{-11}$)

79. VHP−C_O5_2 + VHP−A_rg_7_O7 → sink_50 ($k = 3.20 \times 10^{-11}$)

80. VHP−C_O5_2 + VHP−A_rg_6_O7 → sink_51 ($k = 3.20 \times 10^{-11}$)

81. VHP−C_O5_2 + VHP−A_O7 → sink_52 ($k = 3.20 \times 10^{-11}$)

82. VHP−C_O5_2 + VHP−A_O5 → sink_53 ($k = 3.20 \times 10^{-11}$)

83. VHP−C_O5_2 + VHP−B_O5 → sink_54 ($k = 3.20 \times 10^{-11}$)

84. VHP−C_O5_2 + VHP−B_O7 → sink_55 ($k = 3.20 \times 10^{-11}$)

85. VHP−C_O5_2 → VHP−C_O5_2_rad ($k = 5.79 \times 10^{-02}$)

86. VHP−C_O5_2_rad → VHP−C_O7_2 ($k = 1.00 \times 10^{+07}$)

87. 2 VHP−C_O7_2 → sink_56 ($k = 3.20 \times 10^{-11}$)

88. VHP−C_O7_2 + VHP−C_O5_2 → sink_57 ($k = 3.20 \times 10^{-11}$)

89. VHP−C_O7_2 + VHP−C_O7_h_scram → sink_58 ($k = 3.20 \times 10^{-11}$)

90. VHP−C_O7_2 + VHP−C_O7_1 → sink_59 ($k = 3.20 \times 10^{-11}$)

91. VHP−C_O7_2 + VHP−C_O5_1 → sink_60 ($k = 3.20 \times 10^{-11}$)

92. VHP−C_O7_2 + VHP−A_rg_6_O7 → sink_61 ($k = 3.20 \times 10^{-11}$)

93. VHP−C_O7_2 + VHP−A_rg_7_O7 → sink_62 ($k = 3.20 \times 10^{-11}$)

94. VHP−C_O7_2 + VHP−A_O7 → sink_63 ($k = 3.20 \times 10^{-11}$)

95. VHP−C_O7_2 + VHP−A_O5 → sink_64 ($k = 3.20 \times 10^{-11}$)

96. VHP−C_O7_2 + VHP−B_O5 → sink_65 ($k = 3.20 \times 10^{-11}$)

97. VHP−C_O7_2 + VHP−B_O7 → sink_66 ($k = 3.20 \times 10^{-11}$)

98. VHP−C_O7_2 → VHP−C_rg5_O7_rad ($k = 1.72 \times 10^{+01}$)

99. VHP−C_rg5_O7_rad → VHP−C_O9_rad_rg_5 ($k = 1.00 \times 10^{+07}$)

100. VHP−C_O9_rad_rg_5 → sink_67 ($k = 3.20 \times 10^{-11}$)

101. VHP−C_O9_rad_rg_5 + VHP−C_O7_2 → sink_68 ($k = 3.20 \times 10^{-11}$)

102. VHP−C_O9_rad_rg_5 + VHP−C_O5_2 → sink_69 ($k = 3.20 \times 10^{-11}$)

103. VHP−C_O9_rad_rg_5 + VHP−C_O7_h_scram → sink_70 ($k = 3.20 \times 10^{-11}$)

104. VHP−C_O9_rad_rg_5 + VHP−C_O7_1 → sink_71 ($k = 3.20 \times 10^{-11}$)

105. VHP−C_O9_rad_rg_5 + VHP−C_O5_1 → sink_72 ($k = 3.20 \times 10^{-11}$)

106. VHP−C_O9_rad_rg_5 + VHP−A_rg_7_O7 → sink_73 ($k = 3.20 \times 10^{-11}$)

107. VHP−C_O9_rad_rg_5 + VHP−A_rg_6_O7 → sink_74 ($k = 3.20 \times 10^{-11}$)

108. VHP−C_O9_rad_rg_5 + VHP−A_O7 → sink_75 ($k = 3.20 \times 10^{-11}$)

109. VHP−C_O9_rad_rg_5 + VHP−A_O5 → sink_76 ($k = 3.20 \times 10^{-11}$)

110. VHP−C_O9_rad_rg_5 + VHP−B_O5 → sink_77 ($k = 3.20 \times 10^{-11}$)

111. VHP−C_O9_rad_rg_5 + VHP−B_O7 → sink_78 ($k = 3.20 \times 10^{-11}$)

112. VHP−C_O7_2 → VHP−C_rg6_O7_rad ($k = 1.89 \times 10^{-02}$)

113. VHP−C_rg6_O7_rad → VHP−C_O9_rad_rg_6 ($k = 1.00 \times 10^{+07}$)

114. 2 VHP−C_O9_rad_rg_6 → sink_79 ($k = 3.20 \times 10^{-11}$)

115. VHP−C_O9_rad_rg_6 + VHP−C_O9_rad_rg_5 → sink_80 ($k = 3.20 \times 10^{-11}$)

116. VHP−C_O9_rad_rg_6 + VHP−C_O7_2 → sink_81 ($k = 3.20 \times 10^{-11}$)

117. $\mathrm{VHP{-}C\_O9\_rad\_rg\_6 + VHP{-}C\_O5\_2 \rightarrow sink\_82}$ ($k = 3.20 \times 10^{-11}$)

118. $\mathrm{VHP{-}C\_O9\_rad\_rg\_6 + VHP{-}C\_O7\_h\_scram \rightarrow sink\_83}$ ($k = 3.20 \times 10^{-11}$)

119. $\mathrm{VHP{-}C\_O9\_rad\_rg\_6 + VHP{-}C\_O7\_1 \rightarrow sink\_84}$ ($k = 3.20 \times 10^{-11}$)

120. $\mathrm{VHP{-}C\_O9\_rad\_rg\_6 + VHP{-}C\_O5\_1 \rightarrow sink\_85}$ ($k = 3.20 \times 10^{-11}$)

121. $\mathrm{VHP{-}C\_O9\_rad\_rg\_6 + VHP{-}A\_rg\_6\_O7 \rightarrow sink\_86}$ ($k = 3.20 \times 10^{-11}$)

122. $\mathrm{VHP{-}C\_O9\_rad\_rg\_6 + VHP{-}A\_rg\_7\_O7 \rightarrow sink\_87}$ ($k = 3.20 \times 10^{-11}$)

123. $\mathrm{VHP{-}C\_O9\_rad\_rg\_6 + VHP{-}A\_O7 \rightarrow sink\_88}$ ($k = 3.20 \times 10^{-11}$)

124. $\mathrm{VHP{-}C\_O9\_rad\_rg\_6 + VHP{-}A\_O5 \rightarrow sink\_89}$ ($k = 3.20 \times 10^{-11}$)

125. $\mathrm{VHP{-}C\_O9\_rad\_rg\_6 + VHP{-}B\_O5 \rightarrow sink\_90}$ ($k = 3.20 \times 10^{-11}$)

126. $\mathrm{VHP{-}C\_O9\_rad\_rg\_6 + VHP{-}B\_O7 \rightarrow sink\_91}$ ($k = 3.20 \times 10^{-11}$)

Species nomenclature: VHP-A, VHP-B, and VHP-C denote intermediates originating from the Syn-CI-1, Anti-CI-2, and Anti-CI-2A pathways, respectively. O_3, O_5, O_7, and O_9 indicate the number of oxygen atoms in the corresponding peroxy radical species. The labels *rad* and *mol* denote carbon-centered radical and closed-shell species, respectively, while *rg_5*, *rg_6*, and *rg_7* indicate five-, six-, and seven-membered ring-formation pathways. O_5_1 and O_5_2 denote two distinct O_5 peroxy radical isomers formed from VHP-C. The suffix *h_scram* refers to hydrogen scrambling, and sink species represent generic bimolecular termination products.

References

Barua, S., Kumar, A., Seal, P., Bezaatpour, M., Jha, S., Myllys, N., Iyer, S., and Rissanen, M.: Nitric oxide can enhance secondary aerosol precursor formation from aromatic carbonyls, Nature Communications, https://doi.org/10.1038/s41467-026-72628-w, 2026.

Berndt, T., Scholz, W., Mentler, B., Fischer, L., Herrmann, H., Kulmala, M., and Hansel, A.: Bildung von Aufbauprodukten aus den Selbst- und Kreuzreaktionen von RO2-Radikalen in der Atmosphäre, Angewandte Chemie, 130, 3882–3886, https://doi.org/10.1002/ange.201710989, 2018.

Fang, Y., Liu, F., Barber, V. P., Klippenstein, S. J., McCoy, A. B., and Lester, M. I.: Communication: Real time observation of unimolecular decay of Criegee intermediates to OH radical products, The Journal of Chemical Physics, 144, 061 102, https://doi.org/10.1063/1.4941768, 2016.